A STABLE ADDED-MASS PARTITIONED (AMP) ALGORITHM FOR ELASTIC SOLIDS AND INCOMPRESSIBLE FLOW: MODEL PROBLEM ANALYSIS.*

D. A. SERINO†, J. W. BANKS†, W. D. HENSHAW†, AND D. W. SCHWENDEMAN†

Abstract.
An analysis is made of a new partitioned scheme for solving fluid-structure interaction problems involving viscous incompressible flow and compressible elastic-solids. The new scheme is stable, without sub-time-step iterations, even for light solids when added-mass and added-damping effects are large. The fluid is updated with an implicit-explicit (IMEX) fractional-step scheme whereby the velocity is advanced in one step, treating the viscous terms implicitly, and the pressure is computed in a second step. The key components of the scheme are a Robin (mixed) interface condition for the fluid pressure, and impedance based interface conditions for the velocity. While the impedance for the solid is well defined, the fluid impedance is not, and a semi-discrete local-analysis is used to inform this choice. The properties of the new scheme are analyzed and numerical results are presented to confirm the stability and accuracy of the scheme.

Key words. fluid-structure interaction, incompressible Navier-Stokes, partitioned schemes, added-mass, elastic solids

AMS subject classifications. 65M12, 74F10, 74S10, 76M20, 76D99

1. Introduction.

We consider the numerical solution of fluid-structure interaction (FSI) problems involving incompressible viscous fluids coupled to bulk elastic solids. Such problems arise in many scientific and engineering applications including flow-induced vibrations of structures (i.e., aircraft wings, undersea cables, wind turbines, and bridges), and blood flow in arteries and veins. FSI algorithms can either be categorized as monolithic schemes, where the numerical solutions for the fluid and solid are advanced implicitly as one large system, or partitioned schemes, where the solutions are advanced sequentially. Partitioned schemes are generally more modular and computationally efficient than monolithic schemes. However, depending on the implementation of the fluid-solid interface conditions (which need to be partitioned between the fluid and solid), partitioned schemes may suffer from instabilities, especially for light solids when added-mass effects are large. Typically, partitioned schemes based on traditional Dirichlet-Neumann coupling use under-relaxed sub-time-step iterations together with some acceleration technique to overcome instabilities (at the cost of degrading performance), see for example, [19, 21]. Reduction of sub-iterations can also be achieved by considering, for example, Robin-Neumann or Robin-Robin coupling [26, 12, 2, 22, 15, 14, 13, 16, 3, 23]. Generally the number of sub-time-step iterations increases as the solid becomes lighter, and thus it would be advantageous to have a scheme that does not require sub-iterations. The goal of our current work is to develop such a robust partitioned scheme, without the need for sub-iterations.

In recent work [6], we developed a new class of Added-Mass Partitioned (AMP) algorithms for FSI problems coupling incompressible flow and elastic solids that are stable without sub-iterations. The algorithms in [6] were applied to model problems with infinitesimal interface displacements. The principal goals of the current

*Submitted to the editors DATE.

Funding: This research was supported by the National Science Foundation under grants DGE-1744655, DMS-1519934, and DMS-1818926, as well as by DOE contracts from the ASCR Applied Math Program.

†Department of Mathematical Sciences, Rensselaer Polytechnic Institute, Troy, NY 12180, USA (serind@rpi.edu, banksj3@rpi.edu, henshw@rpi.edu, schwed@rpi.edu).

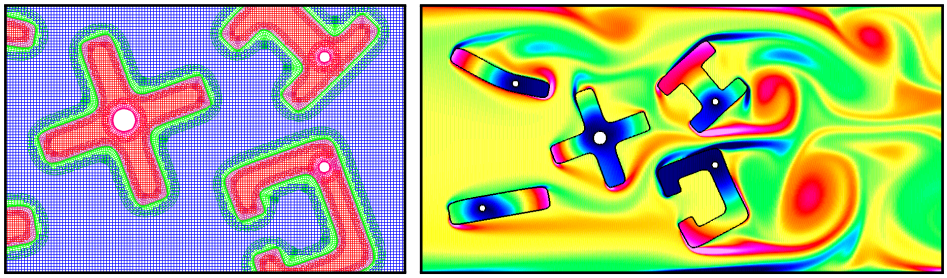

FIG. 1. *Flow past five deformable bodies in a fluid channel computed with the new AMP scheme. Left: overset grids for the fluid and solid domains. Right: contours of the vorticity in the fluid and norm of the displacement in the solids.*

work are to extend the original scheme to finite deformations, and to replace the explicit fluid solver with a fractional-step IMEX scheme, where the viscous terms are treated implicitly. In the explicit scheme, the time step is chosen proportional to the square of the grid spacing. However, the IMEX scheme has a larger stability region so that the time step can be chosen proportional to the grid spacing. This can be a significant advantage when the viscous terms are stiff, such as when fine grids are used near boundaries to resolve boundary layers. The key components of the AMP algorithm are a Robin (mixed) interface condition for the fluid pressure and impedance-based interface conditions for the velocity. While the impedance for the solid is well defined, the impedance for the incompressible fluid is not. A local analysis of the semi-discrete equations for an FSI model problem is performed which reveals that the fluid impedance has an inertial component for treating added-mass instabilities and a viscous component for treating added-damping instabilities. The formula for the fluid impedance is new, and its use is critical for the stability of the AMP algorithm when the viscous CFL number becomes large and added-damping effects are significant. The properties of the new scheme are analyzed for a fundamental FSI model problem, and numerical results are presented to confirm the stability and accuracy of the scheme. The companion paper [24] presents the extension of the new AMP algorithm to treat more complex configurations using overlapping grids, such as the example shown in Figure 1. Our related work describes AMP algorithms for other FSI problems involving incompressible viscous flow coupled to thin elastic structures [7, 20] and rigid bodies [8, 9, 10].

We remark that the AMP algorithm described here was devised through numerical experimentation and the study of suitable model problems, as well as through our experience with other FSI regimes. This strategy, based on gaining insight through an analysis of model problems, has proved to be effective in this work and other cases, and complements more general approaches such as those based on energy estimates. Although the analysis presented here does not rigorously prove results for the general FSI problem, it does provide valuable insight into the approach, as well as a justification for the success of the numerical results presented here and in [24] for more general configurations.

2. Governing equations. We consider the coupled evolution of an incompressible fluid and a linear elastic solid. The fluid occupies the domain $\mathbf{x} \in \Omega(t)$, where $\mathbf{x} = (x_1, x_2, x_3)$ is a vector of physical coordinates and t is time. The velocity-pressure

form of the incompressible Navier-Stokes equations is given by

$$\rho \mathbf{v}_t + \rho(\mathbf{v}\cdot\nabla)\mathbf{v} + \nabla p = \mu\Delta\mathbf{v}, \qquad \mathbf{x}\in\Omega(t), \tag{2.1a}$$

$$\Delta p = -\rho\nabla\mathbf{v} : (\nabla\mathbf{v})^T, \qquad \mathbf{x}\in\Omega(t), \tag{2.1b}$$

where $\mathbf{v}(\mathbf{x},t)$ is the velocity, $p(\mathbf{x},t)$ is the pressure, ρ is the (constant) density, and μ is the (constant) dynamic viscosity. The fluid stress tensor is given by $\boldsymbol{\sigma} = -p\mathbf{I} + \boldsymbol{\tau}$ where $\mathbf{I}$ is the identity matrix and $\boldsymbol{\tau}(\mathbf{x},t) = \mu\left(\nabla\mathbf{v} + \left(\nabla\mathbf{v}\right)^T\right)$ is the viscous stress tensor.

The equations for the solid are written in terms of the Lagrangian coordinate $\bar{\mathbf{x}} = (\bar{x}_1, \bar{x}_2, \bar{x}_3)$ for a reference configuration $\bar{\mathbf{x}} \in \bar{\Omega}_0$ at $t = 0$. (An overbar is used here and elsewhere to denote quantities associated with the solid.) The position of the solid in physical space is determined by the mapping $\mathbf{x} = \bar{\mathbf{x}} + \bar{\mathbf{u}}(\bar{\mathbf{x}},t)$, where $\bar{\mathbf{u}}(\bar{\mathbf{x}},t)$ is the displacement of the solid. The Cauchy stress tensor $\bar{\boldsymbol{\sigma}}(\bar{\mathbf{x}},t)$ for a linearly-elastic solid is defined by $\bar{\boldsymbol{\sigma}} = \bar{\lambda}(\nabla_{\bar{\mathbf{x}}}\cdot\bar{\mathbf{u}})\mathbf{I} + \bar{\mu}\big(\nabla_{\bar{\mathbf{x}}}\bar{\mathbf{u}} + (\nabla_{\bar{\mathbf{x}}}\bar{\mathbf{u}})^T\big)$, where $\bar{\lambda}$ and $\bar{\mu}$ are Lamé parameters (taken to be constants). The solid equations are considered as a first-order system of PDEs in time and space, following [1], and are given by

$$\bar{\mathbf{u}}_t = \bar{\mathbf{v}}, \qquad \bar{\mathbf{x}}\in\bar{\Omega}_0, \tag{2.2a}$$

$$\bar{\rho}\bar{\mathbf{v}}_t = \nabla_{\bar{\mathbf{x}}}\cdot\bar{\boldsymbol{\sigma}}, \qquad \bar{\mathbf{x}}\in\bar{\Omega}_0, \tag{2.2b}$$

$$\bar{\boldsymbol{\sigma}}_t = \bar{\lambda}(\nabla_{\bar{\mathbf{x}}}\cdot\bar{\mathbf{v}})\mathbf{I} + \bar{\mu}\left(\nabla_{\bar{\mathbf{x}}}\bar{\mathbf{v}} + (\nabla_{\bar{\mathbf{x}}}\bar{\mathbf{v}})^T\right), \qquad \bar{\mathbf{x}}\in\bar{\Omega}_0, \tag{2.2c}$$

where $\bar{\mathbf{v}}(\bar{\mathbf{x}},t)$ is the velocity of the solid, and $\bar{\rho}$ is its density (assumed constant).

The fluid and solid are coupled at an interface described by $\mathbf{x}\in\Gamma(t)$ in physical space and $\bar{\mathbf{x}}\in\bar{\Gamma}_0$ in the corresponding reference space. Along the interface, which is assumed smooth, the following matching conditions hold:

$$\mathbf{v} = \bar{\mathbf{v}}, \qquad \boldsymbol{\sigma}\mathbf{n} = \bar{\boldsymbol{\sigma}}\mathbf{n}, \qquad \mathbf{x}\in\Gamma(t), \tag{2.3}$$

where $\mathbf{n}(\mathbf{x},t)$ is the outward unit normal to the fluid domain. Suitable boundary conditions are applied on the boundaries of the fluid and solid domains not included in $\Gamma(t)$, and initial conditions on $\mathbf{v}$, $\bar{\mathbf{u}}$ and $\bar{\mathbf{v}}$ are set to close the problem.

3. AMP interface conditions and algorithm. In this section, we derive the AMP interface conditions at a continuous level and discuss their implementation in the AMP algorithm. The derivation follows the work in [6], but there are important modifications required to accommodate the IMEX fractional-step scheme used in the AMP algorithm to efficiently advance the fluid. These modifications are guided by a consideration of the behavior of the AMP interface conditions in the limits of very light and very heavy solids.

3.1. AMP interface conditions. The starting point for the derivation is the matching conditions involving velocity and stress in (2.3). Following [6], a linear combination of these conditions are expressed in terms of Riemann variables corresponding to the the outgoing solid characteristics, i.e.

$$-p + \mathbf{n}^T\boldsymbol{\tau}\mathbf{n} + \bar{z}_p\mathbf{n}^T\mathbf{v} = \mathbf{n}^T\bar{\boldsymbol{\sigma}}\mathbf{n} + \bar{z}_p\mathbf{n}^T\bar{\mathbf{v}}, \qquad \mathbf{x}\in\Gamma(t), \tag{3.1a}$$

$$\mathbf{t}_m^T\boldsymbol{\tau}\mathbf{n} + \bar{z}_s\mathbf{t}_m^T\mathbf{v} = \mathbf{t}_m^T\bar{\boldsymbol{\sigma}}\mathbf{n} + \bar{z}_s\mathbf{t}_m^T\bar{\mathbf{v}}, \quad m = 1,2, \qquad \mathbf{x}\in\Gamma(t), \tag{3.1b}$$

where $\mathbf{n}$ is the unit normal, $\mathbf{t}_m$, $m = 1,2$, are mutually orthogonal unit vectors tangent to the interface. The Riemann variables in the solid are given by the right-hand side

of (3.1), and can be obtained from the first-order equations in (2.2b)–(2.2c) projected onto the normal to the interface. The impedances, $\bar{z}_p = \bar{\rho}\bar{c}_p$ and $\bar{z}_s = \bar{\rho}\bar{c}_s$, involve the characteristic velocities of the solid given by $\bar{c}_p = \sqrt{(\bar{\lambda} + 2\bar{\mu})/\bar{\rho}}$ and $\bar{c}_s = \sqrt{\bar{\mu}/\bar{\rho}}$. In the AMP algorithm, the conditions in (3.1) are interpreted as providing interface conditions for the fluid in terms of the outgoing characteristic quantities of the solid, assumed known from a previous stage of the algorithm. While these conditions, along with $\nabla \cdot \mathbf{v} = 0$ for $\mathbf{x} \in \Gamma(t)$, are sufficient conditions for the fluid equations in velocity-pressure form, a further manipulation is required to obtain suitable conditions to be used for the fractional-step solver. The objective is to separate the conditions in (3.1) to obtain conditions to be used in the IMEX time-stepping scheme for the fluid velocity and pressure.

For the Poisson problem for the fluid pressure, the interface condition in (3.1a) is used with the momentum equation in (2.1a) to derive a Robin condition for the pressure that balances accelerations. The momentum equation involves the acceleration of the fluid, and this quantity may be obtained on the moving fluid-solid interface using the Taylor approximation

$$\mathbf{v}(\mathbf{x}, t - \Delta t)\Big|_{\mathbf{x}=\mathcal{P}(t-\Delta t)} \approx \big(\mathbf{v}(\mathbf{x}, t) - \Delta t D_t \mathbf{v}(\mathbf{x}, t)\big)\Big|_{\mathbf{x}=\mathcal{P}(t)}, \tag{3.2}$$

where $D_t = \partial_t + \mathbf{v}\cdot\nabla$ is the material derivative, $\mathcal{P}(t)$ is a point on the moving interface and Δt is a time-step. The corresponding approximation for the solid is

$$\bar{\mathbf{v}}(\bar{\mathbf{x}}, t - \Delta t)\Big|_{\bar{\mathbf{x}}=\bar{\mathcal{P}}_0} \approx \big(\bar{\mathbf{v}}(\bar{\mathbf{x}}, t) - \Delta t \bar{\mathbf{v}}_t(\bar{\mathbf{x}}, t)\big)\Big|_{\bar{\mathbf{x}}=\bar{\mathcal{P}}_0}, \tag{3.3}$$

where $\bar{\mathcal{P}}_0$ is the Lagrangian position associated with $\mathcal{P}(t)$. Using (3.2) and (3.3) in (3.1a), and assuming the fluid and solid velocities match on the interface at times $t - \Delta t$ and t, we obtain

$$-p + \mathbf{n}^T \boldsymbol{\tau}\mathbf{n} + \bar{z}_p \Delta t \mathbf{n}^T D_t \mathbf{v} = \mathbf{n}^T \bar{\boldsymbol{\sigma}}\mathbf{n} + \bar{z}_p \Delta t \mathbf{n}^T \bar{\mathbf{v}}_t, \qquad \mathbf{x} \in \Gamma(t).$$

We may now eliminate the fluid acceleration using (2.1a) to obtain the following Robin condition for the fluid pressure:

$$-p - \frac{\bar{z}_p \Delta t}{\rho}\partial_n p = \mathbf{n}^T(\bar{\boldsymbol{\sigma}}\mathbf{n} - \boldsymbol{\tau}\mathbf{n}) + \bar{z}_p \Delta t \mathbf{n}^T\big(\bar{\mathbf{v}}_t + \nu \nabla \times \nabla \times \mathbf{v}\big), \qquad \mathbf{x} \in \Gamma(t), \tag{3.4}$$

where $\partial_n = \mathbf{n} \cdot \nabla$ is the normal derivative and $\nu = \mu/\rho$ is the kinematic viscosity of the fluid. Following [17], we have used the identity, $\Delta \mathbf{v} = -\nabla \times \nabla \times \mathbf{v}$, noting that $\nabla \cdot \mathbf{v} = 0$, to replace $\Delta \mathbf{v}$ on the right-hand side of (3.4) in favor of the curl-curl operator. This is done for improved stability of the fractional-step scheme. The condition in (3.4), along with suitable conditions for $\mathbf{x} \in \partial\Omega(t) \backslash \Gamma(t)$, is used for the Poisson equation in (2.1b) for the pressure.

As was noted in [6], the remaining interface conditions in (3.1b), together with the continuity equation, can be used as boundary conditions to advance the fluid velocity. This was found to be an effective approach for an explicit integration of the momentum equations. To ensure that the fluid velocity and tractions match at the end of the time step, an interface projection is performed to give a common interface velocity $\mathbf{v}^I$ and interface traction $\boldsymbol{\sigma}^I \mathbf{n}$. In analogy to the interface projection used for compressible fluids in [11, 5, 4], which is based on a characteristic analysis, the

projection for incompressible fluids is also proposed to be of the form of an impedance-weighted average. A compact definition of this projection operator is given by

$$\mathbf{w}^I = \mathcal{Z}_I(z_f, \mathbf{v}, \boldsymbol{\sigma}, \bar{z}_p, \bar{z}_s, \bar{\mathbf{v}}, \bar{\boldsymbol{\sigma}}) = (\mathbf{n}^T\mathbf{w}^I)\mathbf{n} + \sum_{m=1}^{2} (\mathbf{t}_m^T\mathbf{w}^I)\mathbf{t}_m,$$

$$\mathbf{n}^T\mathbf{w}^I \stackrel{\text{def}}{=} \frac{1}{z_f + \bar{z}_p}\big\{z_f\mathbf{n}^T\mathbf{v} + \bar{z}_p\mathbf{n}^T\bar{\mathbf{v}} + \mathbf{n}^T(\bar{\boldsymbol{\sigma}}\mathbf{n} - \boldsymbol{\sigma}\mathbf{n})\big\},$$

$$\mathbf{t}_m^T\mathbf{w}^I \stackrel{\text{def}}{=} \frac{1}{z_f + \bar{z}_s}\big\{z_f\mathbf{t}_m^T\mathbf{v} + \bar{z}_s\mathbf{t}_m^T\bar{\mathbf{v}} + \mathbf{t}_m^T(\bar{\boldsymbol{\sigma}}\mathbf{n} - \boldsymbol{\sigma}\mathbf{n})\big\}, \quad m = 1, 2.$$

In terms of $\mathcal{Z}_I$, the velocity and stress projections are

$$\mathbf{v}^I = \mathcal{Z}_I(z_f, \mathbf{v}, \boldsymbol{\sigma}, \bar{z}_p, \bar{z}_s, \bar{\mathbf{v}}, \bar{\boldsymbol{\sigma}}), \tag{3.6a}$$

$$\boldsymbol{\sigma}^I\mathbf{n} = \mathcal{Z}_I(z_f^{-1}, \boldsymbol{\sigma}, \mathbf{v}, \bar{z}_p^{-1}, \bar{z}_s^{-1}, \bar{\boldsymbol{\sigma}}, \bar{\mathbf{v}}), \tag{3.6b}$$

noting the order of arguments for $\boldsymbol{\sigma}^I\mathbf{n}$. These projections introduce a *fluid impedance*, z_f, which is well defined for compressible fluids, but has no obvious definition for incompressible fluids. However, a local analysis of a semi-discrete approximation to the governing equations given in Section 4 suggests a form for z_f given by

$$z_f \stackrel{\text{def}}{=} \mathcal{C}_{\text{AM}}\Big(\frac{\rho h}{\Delta t}\Big) + \mathcal{C}_{\text{AD}}\Big(\frac{\mu}{h}\Big), \tag{3.7}$$

where h is an appropriate mesh spacing and $(\mathcal{C}_{\text{AM}}, \mathcal{C}_{\text{AD}})$ are constants whose approximate values are provided by the analysis.

For the IMEX scheme considered here, a further modification of the previous approach in [6] is required in the implementation of the interface conditions for the fluid velocity. The issue is informed by considering the limits of very light and heavy solids. In the limit of a very light solid ($\bar{z}_p, \bar{z}_s \to 0$), for example, the Robin condition in (3.4) becomes a Dirichlet condition for the pressure, while the interface conditions in (3.1b) reduce to matching conditions involving the shear stress of the fluid. The latter conditions, along with the continuity constraint, provide Neumann conditions on the fluid velocity. These conditions for the fluid pressure and velocity correspond to those for a free surface, and the latter are suitable for the implicit solution of the fluid velocity in the IMEX fractional-step scheme.

The difficulty is revealed in the limit of a very heavy solid ($\bar{z}_p, \bar{z}_s \to \infty$). In this limit, the Robin condition in (3.4) becomes a Neumann condition for the fluid pressure balancing the acceleration of the interface as determined by the solid. This condition is analogous to the usual Neumann boundary condition for the pressure at a rigid boundary obtained from the fluid momentum equations as a compatibility condition (see [17] for example). The interface conditions in (3.1b) reduce to matching conditions involving the tangential components of velocity. However, the matching condition on the normal component of velocity, $\mathbf{n}^T\mathbf{v} = \mathbf{n}^T\bar{\mathbf{v}}$, implied by (3.1a) in the limit of a heavy solid has been lost in the derivation of (3.4). A remedy can be obtained by using the interface projection for the normal component of the velocity in (3.6) as a boundary condition for the implicit solution of the fluid velocity in the IMEX fractional-step scheme. The implementation of this approach is described next in the discussion of the AMP algorithm.

3.2. AMP algorithm. Algorithm 3.1 provides a concise description of the AMP time-stepping scheme (see [24] for additional details of the implementation of the

algorithm). The algorithm advances the solution from a time t^n to $t^{n+1} = t^n + \Delta t$. It is assumed that the fluid domain is represented by a grid consisting of interior points $\mathbf{i} \in \Omega_h$, boundary points $\mathbf{i} \in \partial\Omega_h$ and interface points $\mathbf{i} \in \Gamma_h$, where $\mathbf{i} = (i_1, i_2, i_3)$ is a multi-index. Similarly, the solid reference domain is covered by a grid with interior points $\bar{\mathbf{i}} \in \bar{\Omega}_h$, boundary points $\bar{\mathbf{i}} \in \partial\bar{\Omega}_h$ and interface points $\bar{\mathbf{i}} \in \bar{\Gamma}_h$. Discrete operators, such as ∇_h and Δ_h, denote approximations of the corresponding differential operators on the grid.

Algorithm 3.1 Added-mass partitioned (AMP) scheme

// Predictor steps

1. Predict solid:
$$\begin{cases} \bar{\mathbf{u}}_{\bar{\mathbf{i}}}^{(p)} = \bar{\mathbf{u}}_{\bar{\mathbf{i}}}^{n} + \Delta t \bar{\mathbf{v}}_{\bar{\mathbf{i}}}^{n} + \frac{\Delta t^2}{2\bar{\rho}} \bar{\nabla}_h \cdot \bar{\boldsymbol{\sigma}}_{\bar{\mathbf{i}}}^{n}, & \bar{\mathbf{i}} \in \bar{\Omega}_h. \\ \bar{\mathbf{q}}_{\bar{\mathbf{i}}}^{(p)} = \bar{\mathbf{q}}_{\bar{\mathbf{i}}}^{n} - \Delta t \sum_{m=1}^{3} \frac{1}{\Delta \bar{x}_m} \left(\bar{\mathbf{F}}^{+}_{m,\,\bar{\mathbf{i}}} - \bar{\mathbf{F}}^{-}_{m,\,\bar{\mathbf{i}}} \right), & \bar{\mathbf{i}} \in \bar{\Omega}_h, \end{cases}$$

2. Predict fluid grid: advance fluid grid to t^{n+1} using $\bar{\mathbf{u}}_{\bar{\mathbf{i}}}^{(p)}$ for $\bar{\mathbf{i}} \in \bar{\Gamma}_h$, and compute grid velocity.

3. Predict fluid velocity:
$$\begin{cases} \mathbf{v}_{\mathbf{i}}^{(p)} = \mathbf{v}_{\mathbf{i}}^{n} + \frac{\Delta t}{2}\left(3\mathbf{N}_h(\mathbf{v}_{\mathbf{i}}^{n}, p_{\mathbf{i}}^{n}) - \mathbf{N}_h(\mathbf{v}_{\mathbf{i}}^{n-1}, p_{\mathbf{i}}^{n-1})\right) + \frac{\Delta t}{2}\left(\mathbf{L}_h(\mathbf{v}_{\mathbf{i}}^{(p)}) + \mathbf{L}_h(\mathbf{v}_{\mathbf{i}}^{n})\right), & \mathbf{i} \in \Omega_h \backslash \Gamma_h, \\ \mathbf{t}_m^T \boldsymbol{\tau}_{\mathbf{i}}^{(p)} \mathbf{n} + \bar{z}_s \mathbf{t}_m^T \mathbf{v}_{\mathbf{i}}^{(p)} = \mathbf{t}_m^T \bar{\boldsymbol{\sigma}}_{\bar{\mathbf{i}}}^{(p)} \mathbf{n} + \bar{z}_s \mathbf{t}_m^T \bar{\mathbf{v}}_{\bar{\mathbf{i}}}^{(p)}, & \mathbf{i} \in \Gamma_h,\ \bar{\mathbf{i}} \in \bar{\Gamma}_h, \\ \nabla_h \cdot \mathbf{v}_{\mathbf{i}}^{(p)} = 0, & \mathbf{i} \in \Gamma_h, \\ \mathbf{n}^T \mathbf{v}_{\mathbf{i}}^{(p)} = \frac{z_f}{z_f + \bar{z}_p} \mathbf{n}^T \mathbf{V}_h^p(\mathbf{v}_{\mathbf{i}}^{(p)}) + \frac{\bar{z}_p}{z_f + \bar{z}_p} \mathbf{n}^T \bar{\mathbf{v}}_{\bar{\mathbf{i}}}^{(p)}, \quad \mathbf{t}_m^T \mathbf{v}_{\mathbf{i}}^{(p)} = \mathbf{t}_m^T \mathbf{V}_h^p(\mathbf{v}_{\mathbf{i}}^{(p)}), & \mathbf{i} \in \Gamma_h,\ \bar{\mathbf{i}} \in \bar{\Gamma}_h, \\ \text{Velocity boundary conditions on } \partial\Omega_h \backslash \Gamma_h. \end{cases}$$

4. Predict fluid pressure:
$$\begin{cases} \Delta_h p_{\mathbf{i}}^{(p)} = -\rho \nabla_h \mathbf{v}_{\mathbf{i}}^{(p)} : \left(\nabla_h \mathbf{v}_{\mathbf{i}}^{(p)}\right)^T + \alpha_{\mathbf{i}} \nabla_h \cdot \mathbf{v}_{\mathbf{i}}^{(p)}, & \mathbf{i} \in \Omega_h, \\ -p_{\mathbf{i}}^{(p)} - \frac{\bar{z}_p \Delta t}{\rho} (\mathbf{n} \cdot \nabla_h) p_{\mathbf{i}}^{(p)} = \mathbf{n}^T \left(\bar{\boldsymbol{\sigma}}_{\bar{\mathbf{i}}}^{(p)} \mathbf{n} - \boldsymbol{\tau}_{\mathbf{i}}^{(p)} \mathbf{n} \right) & \\ \qquad + \bar{z}_p \Delta t \mathbf{n}^T \left((\bar{\mathbf{v}}_t)_{\bar{\mathbf{i}}}^{(p)} + \nu \nabla_h \times \nabla_h \times \mathbf{v}_{\mathbf{i}}^{(p)} \right), & \mathbf{i} \in \Gamma_h,\ \bar{\mathbf{i}} \in \bar{\Gamma}_h, \\ \text{Pressure boundary conditions on } \partial\Omega_h \backslash \Gamma_h. \end{cases}$$

5. Project solid interface for $\bar{\mathbf{i}} \in \bar{\Gamma}_h, \mathbf{i} \in \Gamma_h$.
$$\begin{cases} \bar{\mathbf{v}}_{\bar{\mathbf{i}}}^{I} = \mathcal{Z}_I(z_f, \mathbf{v}_{\mathbf{i}}^{(p)}, \boldsymbol{\sigma}_{\mathbf{i}}^{(p)}, \bar{z}_p, \bar{z}_s, \bar{\mathbf{v}}_{\bar{\mathbf{i}}}^{(p)}, \bar{\boldsymbol{\sigma}}_{\bar{\mathbf{i}}}^{(p)}) \\ \bar{\boldsymbol{\sigma}}_{\bar{\mathbf{i}}}^{I} \mathbf{n} = \mathcal{Z}_I(z_f^{-1}, \boldsymbol{\sigma}_{\mathbf{i}}^{(p)}, \mathbf{v}_{\mathbf{i}}^{(p)}, \bar{z}_p^{-1}, \bar{z}_s^{-1}, \bar{\boldsymbol{\sigma}}_{\bar{\mathbf{i}}}^{(p)}, \bar{\mathbf{v}}_{\bar{\mathbf{i}}}^{(p)}) \\ \bar{\mathbf{v}}_{\bar{\mathbf{i}}}^{(p)} \leftarrow \bar{\mathbf{v}}_{\bar{\mathbf{i}}}^{I}, \quad \bar{\boldsymbol{\sigma}}_{\bar{\mathbf{i}}}^{(p)} \mathbf{n} \leftarrow \bar{\boldsymbol{\sigma}}_{\bar{\mathbf{i}}}^{I} \mathbf{n}, \\ \text{Apply solid boundary conditions and set all ghost points.} \end{cases}$$

// Corrector steps

6. Correct fluid grid: recompute grid velocity using $\bar{\mathbf{v}}_{\bar{\mathbf{i}}}^{I}$ for $\bar{\mathbf{i}} \in \bar{\Gamma}_h$.

7. Correct fluid velocity:
$$\begin{cases} \mathbf{v}_{\mathbf{i}}^{n+1} = \mathbf{v}_{\mathbf{i}}^{n} + \frac{\Delta t}{2}\left(\mathbf{N}_h(\mathbf{v}_{\mathbf{i}}^{(p)}, p_{\mathbf{i}}^{(p)}) + \mathbf{N}_h(\mathbf{v}_{\mathbf{i}}^{n}, p_{\mathbf{i}}^{n})\right) + \frac{\Delta t}{2}\left(\mathbf{L}_h(\mathbf{v}_{\mathbf{i}}^{n+1}) + \mathbf{L}_h(\mathbf{v}_{\mathbf{i}}^{n})\right), & \mathbf{i} \in \Omega_h \backslash \Gamma_h, \\ \mathbf{t}_m^T \boldsymbol{\tau}_{\mathbf{i}}^{n+1} \mathbf{n} + \bar{z}_s \mathbf{t}_m^T \mathbf{v}_{\mathbf{i}}^{n+1} = \mathbf{t}_m^T \bar{\boldsymbol{\sigma}}_{\bar{\mathbf{i}}}^{I} \mathbf{n} + \bar{z}_s \mathbf{t}_m^T \bar{\mathbf{v}}_{\bar{\mathbf{i}}}^{I}, & \mathbf{i} \in \Gamma_h,\ \bar{\mathbf{i}} \in \bar{\Gamma}_h, \\ \nabla_h \cdot \mathbf{v}_{\mathbf{i}}^{n+1} = 0, & \mathbf{i} \in \Gamma_h, \\ \mathbf{n}^T \mathbf{v}_{\mathbf{i}}^{n+1} = \frac{z_f}{z_f + \bar{z}_p} \mathbf{n}^T \mathbf{V}_h(\mathbf{v}_{\mathbf{i}}^{n+1}) + \frac{\bar{z}_p}{z_f + \bar{z}_p} \mathbf{n}^T \bar{\mathbf{v}}_{\bar{\mathbf{i}}}^{I}, \quad \mathbf{t}_m^T \mathbf{v}_{\mathbf{i}}^{n+1} = \mathbf{t}_m^T \mathbf{V}_h(\mathbf{v}_{\mathbf{i}}^{n+1}), & \mathbf{i} \in \Gamma_h,\ \bar{\mathbf{i}} \in \bar{\Gamma}_h, \\ \text{Velocity boundary conditions on } \partial\Omega_h \backslash \Gamma_h. \end{cases}$$

8. Correct fluid pressure.
$$\begin{cases} \Delta_h p_{\mathbf{i}}^{n+1} = -\rho \nabla_h \mathbf{v}_{\mathbf{i}}^{n+1} : \left(\nabla_h \mathbf{v}_{\mathbf{i}}^{n+1}\right)^T + \alpha_{\mathbf{i}} \nabla_h \cdot \mathbf{v}_{\mathbf{i}}^{n+1}, & \mathbf{i} \in \Omega_h, \\ -p_{\mathbf{i}}^{n+1} - \frac{\bar{z}_p \Delta t}{\rho} (\mathbf{n} \cdot \nabla_h) p_{\mathbf{i}}^{n+1} = \mathbf{n}^T \left(\bar{\boldsymbol{\sigma}}_{\bar{\mathbf{i}}}^{I} \mathbf{n} - \boldsymbol{\tau}_{\mathbf{i}}^{n+1} \mathbf{n} \right) & \\ \qquad + \bar{z}_p \Delta t \mathbf{n}^T \left((\bar{\mathbf{v}}_t)_{\bar{\mathbf{i}}}^{I} + \nu \nabla_h \times \nabla_h \times \mathbf{v}_{\mathbf{i}}^{n+1} \right), & \mathbf{i} \in \Gamma_h,\ \bar{\mathbf{i}} \in \bar{\Gamma}_h, \\ \text{Pressure boundary conditions on } \partial\Omega_h \backslash \Gamma_h. \end{cases}$$

9. Correct solid interface.
$$\begin{cases} \bar{\mathbf{v}}_{\bar{\mathbf{i}}}^{n+1} = \mathbf{v}_{\mathbf{i}}^{n+1}, & \bar{\mathbf{i}} \in \bar{\Gamma}_h, \mathbf{i} \in \Gamma_h, \\ \bar{\boldsymbol{\sigma}}_{\bar{\mathbf{i}}}^{n+1} \mathbf{n} = \boldsymbol{\sigma}_{\mathbf{i}}^{n+1} \mathbf{n}, & \bar{\mathbf{i}} \in \bar{\Gamma}_h, \mathbf{i} \in \Gamma_h, \\ \text{Reset ghost points corresponding to } \bar{\mathbf{i}} \in \bar{\Gamma}_h. \end{cases}$$

The time-stepping scheme uses a predictor-corrector approach. Steps 1–5 of Algorithm 3.1 describe the predictor steps. Predicted values for the solid displacement

$\bar{\mathbf{u}}_{\bar{\mathbf{i}}}$ are obtained in Step 1 using a Lax-Wendroff-type scheme for (2.2a), while the solid velocity and stress $\bar{\mathbf{q}}_{\bar{\mathbf{i}}} = (\bar{\mathbf{v}}_{\bar{\mathbf{i}}}, \bar{\boldsymbol{\sigma}}_{\bar{\mathbf{i}}})$ are advanced using a Godunov-type scheme for (2.2b) and (2.2c) with numerical fluxes $\bar{\mathbf{F}}^{\pm}_{m,\,\bar{\mathbf{i}}}$ corresponding to the $\bar{x}_m$-direction. In Step 2, the solid displacement is used to compute the deformed fluid grid at time t^{n+1}.

The fluid velocity is predicted in Step 3. Here, $\mathbf{N}_h$ and $\mathbf{L}_h$ represent grid operators associated with the explicit and implicit terms in the velocity update, respectively, given by

$$\mathbf{N}_h(\mathbf{v}_\mathbf{i}, p_\mathbf{i}) \stackrel{\text{def}}{=} -\big((\mathbf{v}_\mathbf{i} - \dot{\mathbf{x}}_\mathbf{i}) \cdot \nabla_h\big)\mathbf{v}_\mathbf{i} - \frac{1}{\rho}\nabla_h\, p_\mathbf{i}, \qquad \mathbf{L}_h(\mathbf{v}_\mathbf{i}) \stackrel{\text{def}}{=} \nu\Delta_h\mathbf{v}_\mathbf{i},$$

where $\dot{\mathbf{x}}_\mathbf{i}$ is the velocity of the grid. The explicit terms are advanced using an Adams-Bashforth scheme, while the implicit terms use Crank-Nicholson. The boundary conditions on the interface makes use of a predicted velocity, coming from the interior equation applied on the boundary, and defined by

$$\mathbf{V}_h^p(\mathbf{v}_\mathbf{i}^{(p)}) \stackrel{\text{def}}{=} \mathbf{v}_\mathbf{i}^n + \frac{\Delta t}{2}\left(3\mathbf{N}_h(\mathbf{v}_\mathbf{i}^n, p_\mathbf{i}^n) - \mathbf{N}_h(\mathbf{v}_\mathbf{i}^{n-1}, p_\mathbf{i}^{n-1})\right) + \frac{\Delta t}{2}\left(\mathbf{L}_h(\mathbf{v}_\mathbf{i}^{(p)}) + \mathbf{L}_h(\mathbf{v}_\mathbf{i}^n)\right).$$

In particular, this velocity is used in the impedance-weighted average condition

$$\mathbf{n}^T\mathbf{v}_\mathbf{i}^{(p)} = \frac{z_f}{z_f + \bar{z}_p}\mathbf{n}^T\mathbf{V}_h^p(\mathbf{v}_\mathbf{i}^{(p)}) + \frac{\bar{z}_p}{z_f + \bar{z}_p}\mathbf{n}^T\bar{\mathbf{v}}_{\bar{\mathbf{i}}}^{(p)}, \qquad \mathbf{i} \in \Gamma_h, \quad \bar{\mathbf{i}} \in \bar{\Gamma}_h, \tag{3.8}$$

which is obtained from the projection in (3.6). Here the the term involving the jump in the stress is dropped (as it is apparently not essential to the scheme and simplifies the implementation, see also [11]). Notice that (3.8) is an implicit condition on $\mathbf{v}_\mathbf{i}^{(p)}$ which appears on the left- and right-hand sides. In the light-solid limit ($\bar{z}_p \to 0$), the boundary condition in (3.8) reduces to $\mathbf{n}^T\mathbf{v}_\mathbf{i}^{(p)} = \mathbf{n}^T\mathbf{V}_h^p(\mathbf{v}_\mathbf{i}^{(p)})$, which simply sets the normal component of the fluid velocity to be equal to that given by the interior time-stepping scheme applied on the boundary. In the heavy-solid limit ($\bar{z}_p \to \infty$), (3.8) becomes $\mathbf{n}^T\mathbf{v}_\mathbf{i}^{(p)} = \mathbf{n}^T\bar{\mathbf{v}}_{\bar{\mathbf{i}}}^{(p)}$, which recovers the desired matching condition. Our later analysis of a viscous model problem (Section 5) and subsequent numerical results (Section 6), verify that the boundary conditions used to advance the fluid velocity in the fractional-step scheme lead to stable and accurate results for all solid densities we have considered.

Steps 4 and 5 complete the set of steps belonging to the predictor stage of the algorithm. The predicted fluid pressure is computed in Step 4 by solving a discrete Poisson problem. This elliptic problem uses a discrete approximation of the Robin condition in (3.4). Finally, interface values for the solid velocity and traction are obtained in Step 5 using the impedance-weighted projections in (3.6). These interface values overwrite the corresponding predicted values of the solid on the boundary.

The set of corrector steps consisting of Steps 6–9 essentially mirror those of the predictor. In an important final Step 9, the solid velocity and traction are set equal to the corrected fluid values.

4. Derivation of the fluid impedance. The focus of this section is an analysis of an FSI problem that guides the choice for the fluid impedance z_f introduced in (3.7) and required in the interface projections (3.6). Previously in [6], the choice of fluid impedance was found to be somewhat arbitrary and a choice was made of $z_f = \rho H/\Delta t$, where H was a measure of the depth of the fluid layer. With the current IMEX scheme, the viscous CFL number, $\Lambda = \nu\Delta t/h^2$, can be large in which case a new choice for

z_f is needed to keep the scheme stable; a carefully chosen model problem is used for this purpose.

Consider an FSI model problem in which the fluid occupies the two-dimensional domain, Ω, given by $0 < x < L$, $y > 0$, while the solid exists on the domain, $\bar{\Omega}_0$, for $0 < x < L$, $y < 0$. The fluid-solid interface, Γ, of length L is linearized about a flat surface, $y = 0$. The equations governing the model problem are

$$\text{Fluid:} \quad \begin{cases} \rho\partial_t \mathbf{v} + \nabla p = \mu\Delta\mathbf{v}, & \mathbf{x} \in \Omega, \\ \Delta p = 0, & \mathbf{x} \in \Omega, \\ \nabla \cdot \mathbf{v} = 0, & \mathbf{x} \in \Gamma, \end{cases} \tag{4.1a}$$

$$\text{Solid:} \quad \begin{cases} \bar{\rho}\partial_t \bar{\mathbf{v}} = \nabla \cdot \bar{\boldsymbol{\sigma}}, & \mathbf{x} \in \bar{\Omega}_0, \\ \partial_t \bar{\boldsymbol{\sigma}} = \bar{\lambda}(\nabla \cdot \mathbf{v})\mathbf{I} + \bar{\mu}(\nabla\mathbf{v} + (\nabla\mathbf{v})^T), & \mathbf{x} \in \bar{\Omega}_0, \end{cases} \tag{4.1b}$$

$$\text{Interface:} \quad \begin{cases} \mathbf{v} = \bar{\mathbf{v}}, & \mathbf{x} \in \Gamma, \\ \boldsymbol{\sigma}\mathbf{n} = \bar{\boldsymbol{\sigma}}\mathbf{n}, & \mathbf{x} \in \Gamma. \end{cases} \tag{4.1c}$$

Solutions of the model problem are assumed to be periodic in x with period equal to L, and bounded as $y \to \pm\infty$. The equations governing the fluid and solid are discretized in the x-direction on a uniform grid, $x_\ell = \ell\Delta x$ for $\ell = 0, 1, \ldots N_x$, with grid spacing $\Delta x = L/N_x$. Since the problem is periodic, each variable can be represented as a discrete Fourier series

$$q(x, y, t) = \sum_{k=-N_x/2}^{N_x/2} e^{2\pi i k x/L} \hat{q}_k(y, t), \qquad x \in [0, L], \tag{4.2}$$

where $\hat{q}_k(y, t)$ are the Fourier coefficient functions and N_x is an integer, assumed to be even for convenience. Taking a finite Fourier transform of the fluid equations in (4.1a) gives

$$\rho\partial_t v_1 + ik_x p = \mu(\partial_y^2 - k_x^2)v_1, \qquad y > 0, \tag{4.3a}$$

$$\rho\partial_t v_2 + \partial_y p = \mu(\partial_y^2 - k_x^2)v_2, \qquad y > 0, \tag{4.3b}$$

$$(\partial_y^2 - k_x^2)p = 0, \qquad y > 0, \tag{4.3c}$$

where $k_x = 2\pi k/L$. The hats and k subscripts on the coefficient functions in (4.3) have been dropped for notational convenience. The equations for the Fourier coefficient functions are now discretized in time. Define the grid functions $\mathbf{v}^n(y) \approx \mathbf{v}(y, t^n)$ and $p^n \approx p(y, t^n)$, where $t^n = n\Delta t$ for a (fixed) time step Δt. An implicit scheme to advance the solution from t^n to t^{n+1}, based on backward-Euler time-stepping, is given by

$$\rho\frac{v_1^{n+1} - v_1^n}{\Delta t} + ik_x p^{n+1} = \mu(\partial_y^2 - k_x^2)v_1^{n+1}, \qquad y > 0, \tag{4.4a}$$

$$\rho\frac{v_2^{n+1} - v_2^n}{\Delta t} + \partial_y p^{n+1} = \mu(\partial_y^2 - k_x^2)v_2^{n+1}, \qquad y > 0, \tag{4.4b}$$

$$(\partial_y^2 - k_x^2)p^{n+1} = 0. \qquad y > 0. \tag{4.4c}$$

Assume that the coefficient functions for the solid variables have been advanced to $t = t^{n+1}$ using an upwind scheme, for example, and that b_p^{n+1} and b_s^{n+1} are, respectively, the normal and tangential components of the outgoing characteristic variables of the

solid at t^{n+1}. Using (3.1), the boundary conditions for the fluid at $y = 0$ take the form

$$-p^{n+1} + \tau_{22}^{n+1} - \bar{z}_p v_2^{n+1} = b_p^{n+1}, \qquad y = 0, \tag{4.5a}$$

$$\tau_{12}^{n+1} - \bar{z}_s v_1^{n+1} = b_s^{n+1}, \qquad y = 0, \tag{4.5b}$$

where the components of the fluid shear stress in (4.5) are given by

$$\tau_{12}^{n+1} = \mu \left(ik_x v_2^{n+1} + \partial_y v_1^{n+1} \right), \qquad \tau_{22}^{n+1} = 2\mu \partial_y v_2^{n+1}.$$

The implicit scheme in (4.4) with boundary conditions in (4.5) at $y = 0$ and boundedness as $y \to \infty$ determine the grid functions for the fluid at t^{n+1} in terms the fluid velocity at t^n and the outgoing solid data (b_p^{n+1}, b_s^{n+1}).

Consider perturbations in the grid functions of the fluid at t^{n+1} for $y > 0$ subject to perturbations in the interface data b_p^{n+1} and b_s^{n+1} at $y = 0$. The variational equations corresponding to (4.4) are

$$\begin{aligned}
\frac{\rho}{\Delta t}\delta V_1 + ik_x \delta P &= \mu(\partial_y^2 - k_x^2)\delta V_1, \qquad && y > 0, \\
\frac{\rho}{\Delta t}\delta V_2 + \partial_y \delta P &= \mu(\partial_y^2 - k_x^2)\delta V_2, && y > 0, \\
(\partial_y^2 - k_x^2)\delta P &= 0, && y > 0,
\end{aligned}$$

where $(\delta V_1, \delta V_2, \delta P)$ are small perturbations corresponding to $(v_1^{n+1}, v_2^{n+1}, p^{n+1})$. Solutions to these equations that remain bounded as $y \to \infty$ are

$$\begin{aligned}
\delta V_1(y) &= -\frac{1}{ik_x}\partial_y \delta V_2(y), \\
\delta V_2(y) &= \delta V_0 e^{-\beta y} + \frac{|k_x|\Delta t \delta P_0}{\rho}\left(e^{-|k_x| y} - e^{-\beta y} \right), \\
\delta P(y) &= \delta P_0 e^{-|k_x| y},
\end{aligned}$$

where $\delta V_0 = \delta V_2(0)$, $\delta P_0 = \delta P(0)$ and $\beta = \sqrt{k_x^2 + \rho/(\mu \Delta t)}$. Substituting the solution for the perturbations of the fluid variables into the variational equations corresponding to (4.5) for the interface conditions leads to the linear system

$$\begin{bmatrix} a_{11} & a_{12} \\ a_{21} & a_{22} \end{bmatrix} \begin{bmatrix} \delta V_0 \\ \delta P_0 \end{bmatrix} = \begin{bmatrix} \delta B_p \\ \delta B_s \end{bmatrix},$$

where $a_{11} = -\mu|k_x|(2\gamma + 1/Z_p)$, $a_{12} = -1 + 2\Lambda(\gamma - 1)$, $a_{21} = i\mu k_x(\gamma^2 + 1 + \gamma/Z_s)$ and $a_{22} = -i\,\mathrm{sgn}(k_x)(1 + \Lambda(\gamma - 1)/Z_s)$. Here, $(\delta B_p, \delta B_s)$ are small perturbations corresponding to (b_p^{n+1}, b_s^{n+1}). The coefficients a_{ij} in the linear system are defined in terms of the dimensionless parameters

$$\Lambda \stackrel{\text{def}}{=} \nu k_x^2 \Delta t, \qquad \gamma \stackrel{\text{def}}{=} \beta/|k_x| = \sqrt{1 + 1/\Lambda}, \qquad Z_\alpha \stackrel{\text{def}}{=} \mu|k_x|/\bar{z}_\alpha, \quad \alpha = p \text{ or } s.$$

The solution of the linear system

$$\delta V_0 = \frac{a_{22}\delta B_p - a_{12}\delta B_s}{a_{11}a_{22} - a_{12}a_{21}}, \qquad \delta P_0 = \frac{a_{11}\delta B_s - a_{21}\delta B_p}{a_{11}a_{22} - a_{12}a_{21}}, \tag{4.8}$$

determines the variation in the interface values of the fluid velocity and pressure in terms of the variations in the outgoing characteristic variables of the solid.

The AMP algorithm uses impedance-weighted averages to set values for the velocity and pressure at the interface. For example, the normal component of velocity at the interface is given by (3.6a). In terms of the variational problem, (3.6a) reduces to $\delta V_0 = -\delta B_p/(z_f + \bar{z}_p)$, assuming that the fluid velocity and stress on the right-hand side are held fixed. In view of the solution in (4.8), we have $(z_f + \bar{z}_p)^{-1} = -a_{22}/(a_{11}a_{22} - a_{12}a_{21})$, which, after some manipulation, gives

$$z_f = \mu|k_x|R, \qquad R \stackrel{\text{def}}{=} 2\gamma + \frac{(\gamma + Z_s(\gamma^2+1))(1-2\Lambda(\gamma-1))}{\Lambda(\gamma-1)(1+Z_s(\gamma+1))}. \tag{4.9}$$

Of particular interest are the limiting cases when the viscous CFL number, Λ, is small and large. A straightforward analysis of the dimensionless parameter R in (4.9) gives $R \sim 1/\Lambda$ for $\Lambda \ll 1$ and $R \sim 2$ for $\Lambda \gg 1$. In view of these limits, consider an approximation to R given by

$$\tilde{R} \stackrel{\text{def}}{=} 1/\Lambda + 2.$$

It is found that $1 \le R/\tilde{R} \le (\sqrt{2}+1)/2 \approx 1.21$ for all (Λ, Z_s), so that the fluid impedance given by

$$z_f = \mu|k_x|\tilde{R} = \mu|k_x|\,(1/\Lambda + 2) = \rho/(|k_x|\Delta t) + 2\mu|k_x|, \tag{4.10}$$

is a good approximation of the more complicated form given in (4.9). The model problem analysis of Section 5 confirms that this choice leads to a stable scheme.

Formula (4.10) provides the generic form of the fluid impedance we use, but it remains to make a choice for k_x so that the approximation can be used for a discrete approximation in physical coordinates (as opposed to the Fourier transformed space). Note that in a discrete approximation, the magnitude of the possible wave numbers k_x appearing in (4.10) are bounded by approximately $1/h$, where h is a measure of the grid spacing in the tangential direction. For the present model problem with the the pseudo-spectral approximation (4.2), for example, we have $|k_x| \le \pi/\Delta x$, while a second-order difference approximation would roughly imply $|k_x| \le 2/\Delta x$. Experience [8] shows that added-damping instabilities are generally caused by relatively high-frequency modes on the grid, and this suggests taking $|k_x| = 1/h$ which leads to a definition of the fluid impedance of the form

$$z_f \stackrel{\text{def}}{=} \mathcal{C}_{\text{AM}}\Big(\frac{\rho\, h}{\Delta t}\Big) + \mathcal{C}_{\text{AD}}\Big(\frac{\mu}{h}\Big),$$

as was done in (3.7). The extensive numerical results in Section 6 and [24] confirm that this is an appropriate choice, and furthermore that the scheme is rather insensitive to the choice of h, $\mathcal{C}_{\text{AM}}$ and $\mathcal{C}_{\text{AD}}$.

5. Stability analysis of an FSI model problem. The stability of the AMP algorithm is explored in the context of an FSI model problem involving a viscous incompressible (Stokes) fluid in contact with a simplified elastic solid. This analysis extends the work in [6] to the case of a viscous fluid where both added-mass and added-damping effects are important, and for an IMEX-type scheme in the fluid.

We will compare the stability of the AMP scheme to that of the traditional partitioned (TP) scheme and the anti-traditional partitioned (ATP) scheme. In the TP scheme, the solid provides a Dirichlet (no-slip) boundary condition for the fluid, and then the fluid supplies a Neumann (traction) boundary condition for the solid. The ATP scheme reverses the role of the solid and fluid. In this scheme, the solid provides a Neumann (traction) boundary condition for the fluid and the fluid supplies a Dirichlet (no-slip) boundary condition for the solid.

5.1. Model problem. The viscous model problem analyzed here is similar to the one discussed in Section 4. An incompressible Stokes fluid satisfies the system of equations in (4.1a) for $\mathbf{x} \in \Omega$. The solid satisfies (4.1b) for $\mathbf{x} \in \bar{\Omega}_0$, but with $\bar{\lambda}$ set equal to $-\bar{\mu}$. While this choice may not correspond to any actual solid, it is a useful choice mathematically as is simplifies the equations for the solid somewhat since the compressive wave speed becomes equal to the shear wave speed, $\bar{c} = \sqrt{\bar{\mu}/\bar{\rho}}$, which is particularly relevant for the viscous model problem. It is convenient to consider the hyperbolic equations for the solid in characteristic form. These equations are

$$\partial_t a_1 - \bar{c}\partial_y a_1 = \bar{c}(\partial_x d - \partial_x b_2), \qquad \mathbf{x} \in \bar{\Omega}_0, \tag{5.1a}$$

$$\partial_t b_1 + \bar{c}\partial_y b_1 = \bar{c}(\partial_x a_2 - \partial_x d), \qquad \mathbf{x} \in \bar{\Omega}_0, \tag{5.1b}$$

$$\partial_t a_2 - \bar{c}\partial_y a_2 = \bar{c}\partial_x b_1, \qquad \mathbf{x} \in \bar{\Omega}_0, \tag{5.1c}$$

$$\partial_t b_2 + \bar{c}\partial_y b_2 = -\bar{c}\partial_x a_1, \qquad \mathbf{x} \in \bar{\Omega}_0, \tag{5.1d}$$

$$\partial_t d = 0, \qquad \mathbf{x} \in \bar{\Omega}_0, \tag{5.1e}$$

where $a_m = \bar{\sigma}_{m2} + \bar{z}\bar{v}_m$ and $b_m = \bar{\sigma}_{m2} - \bar{z}\bar{v}_m$, for $m = 1, 2$ and $\bar{z} = \bar{\rho}\bar{c}$, are the variables associated with the incoming and outgoing characteristics at the interface, respectively, and $d = \bar{\sigma}_{11} + \bar{\sigma}_{22}$. The interface is linearized about a flat surface Γ given by $y = 0$, and the matching conditions between the fluid and the solid are given in (4.1c).

5.2. Discretization. The discretization of the equations in the x-direction follows the approach used previously in Section 4. The equations for the fluid are transformed using the finite Fourier series in (4.2), which results in a system of equations for the corresponding Fourier coefficient functions given in (4.1a). These equations are then discretized in time using an IMEX scheme given by

$$v_1^{n+1} = v_1^n - \frac{ik_x\Delta t}{\rho} p^n + \nu\Delta t\left(-k_x^2 + \partial_y^2\right) v_1^{n+1}, \tag{5.2a}$$

$$v_2^{n+1} = v_2^n - \frac{\Delta t}{\rho}\partial_y p^n + \nu\Delta t\left(-k_x^2 + \partial_y^2\right) v_2^{n+1}, \tag{5.2b}$$

$$\left(-k_x^2 + \partial_y^2\right) p^{n+1} = 0. \tag{5.2c}$$

Here, $v_1^n(y)$, $v_2^n(y)$ and $p^n(y)$ approximate $v_1(y, t^n)$, $v_2(y, t^n)$ and $p(y, t^n)$, respectively, at $t^n = n\Delta t$ for a fixed time step Δt. Recall that $k_x = 2\pi k/L$ and $\nu = \mu/\rho$, and that the hats and k subscripts on the Fourier coefficients have been suppressed. Note that the components of the fluid velocity are advanced in time using (implicit) backward Euler for the viscous terms and (explicit) forward Euler for the pressure gradient terms. An elliptic equation is solved at each time step to update the pressure. It is convenient to keep the discrete equations for the fluid variables continuous in y, and we assume that solutions are bounded as $y \to \infty$.

The characteristic equations for the solid in (5.1) are similarly transformed using the finite Fourier series in (4.2), and then the resulting equations are discretized in time and space using an upwind-type scheme given by

$$a_{1,j}^{n+1} = a_{1,j}^n + \bar{c}\Delta t(a_{1,j+1}^n - a_{1,j}^n)/\Delta y + i\bar{c}k_x\Delta t(d_j^{n+1} - b_{2,j}^{n+1}), \tag{5.3a}$$

$$b_{1,j}^{n+1} = b_{1,j}^n - \bar{c}\Delta t(b_{1,j}^n - b_{1,j-1}^n)/\Delta y + i\bar{c}k_x\Delta t(a_{2,j}^{n+1} - d_j^{n+1}), \tag{5.3b}$$

$$a_{2,j}^{n+1} = a_{2,j}^n + \bar{c}\Delta t(a_{2,j+1}^n - a_{2,j}^n)/\Delta y + i\bar{c}k_x\Delta t\, b_{1,j}^{n+1}, \tag{5.3c}$$

$$b_{2,j}^{n+1} = b_{2,j}^n - \bar{c}\Delta t(b_{2,j}^n - b_{2,j-1}^n)/\Delta y - i\bar{c}k_x\Delta t\, a_{1,j}^{n+1}, \tag{5.3d}$$

$$d_j^{n+1} = d_j^n, \tag{5.3e}$$

where, for example, $a^n_{1,j} \approx a_1(y_j, t^n)$ with $y_j = j\Delta y$. The grid in the y-direction is collocated about the interface at $y = 0$. The terms involving transverse derivatives are treated implicitly to stabilize the pseudo-spectral approximation. For reference, the solid velocity and stress are related to the characteristic variables by $\bar{v}^n_{m,j} = \frac{1}{2\bar{z}}\left(a^n_{m,j} - b^n_{m,j}\right)$, $\bar{\sigma}^n_{m2,j} = \frac{1}{2}\left(a^n_{m,j} + b^n_{m,j}\right)$, $m = 1, 2$. We assume bounded solutions of (5.3) as $y_j \to -\infty$.

5.3. Interface coupling. We explore the stability of partitioned schemes for the model problem that use different interface coupling approaches. For any of the approaches, corresponding to the AMP, TP, and ATP schemes, the discrete equations require a certain number of boundary conditions at the interface. For example, the evolution of the fluid equations in (5.2) require three boundary conditions on the interface, $y = 0$, to determine the interface velocity and pressure. Similarly, the evolution of the solid equations in (5.3) require two boundary conditions at $y = 0$ corresponding to the two incoming characteristic variables.

We first describe the coupling based on the AMP interface conditions given in Section 3. We assume the fluid and solid solutions are known at time t^n. The solid variables are advanced first to t^{n+1} on grid points $j = 0, -1, -2, \ldots$ using the evolution equations in (5.3). The solid interface velocity and stress are computed using

$$\bar{v}^{n+1}_{m,0} = \frac{1}{2\bar{z}}\left(a^{n+1}_{m_0} - b^{n+1}_{m,0}\right), \qquad \bar{\sigma}^{n+1}_{m2,0} = \frac{1}{2}\left(a^{n+1}_{m,0} + b^{n+1}_{m,0}\right), \qquad m = 1, 2.$$

The fluid velocity is advanced using (5.2a)–(5.2b). Two boundary conditions are required at $y = 0$ to obtain the fluid velocity at t^{n+1}. The condition on the outgoing solid tangential characteristic in (3.1b) becomes

$$\mu\left(ik_x v_2^{n+1} + \partial_y v_1^{n+1}\right) - \bar{z} v_1^{n+1} = \bar{\sigma}^{n+1}_{12,0} - \bar{z}\bar{v}^{n+1}_{1,0}, \qquad y = 0. \tag{5.4}$$

The normal component of the velocity is projected to obtain the proper limiting behaviors for heavy and light solids. This condition, taken from (3.8), reduces to

$$v_2^{n+1} = \frac{z_f}{z_f + \bar{z}} V^p(v_2^{n+1}) + \frac{\bar{z}}{z_f + \bar{z}} \bar{v}^{n+1}_{2,0}, \qquad y = 0, \tag{5.5}$$

where the fluid impedance is given by $z_f = \rho/(k_x\Delta t) + 2\mu k_x$, according to the derivation in Section 4. The predicted velocity, $V^p(v_2^{n+1})$, in (5.5) is given by

$$V^p(v_2^{n+1}) = v_2^n - \frac{\Delta t}{\rho}\partial_y p^n - \nu\Delta t\left(k_x^2 v_2^{n+1} + ik_x\partial_y v_1^{n+1}\right), \qquad y = 0. \tag{5.6}$$

This definition is analogous to the definition for $\mathbf{V}^p(\mathbf{v}_\mathbf{i}^{(p)})$ in Section 3, but with the substitution $\partial_y v_2^{n+1} = -ik_x v_1^{n+1}$ noting that $\nabla\cdot\mathbf{v} = 0$ on the boundary. The pressure is updated using (5.2c) along with the AMP pressure condition described in (3.4). For the present scheme, this condition reduces to

$$\begin{aligned} -p^{n+1} + \frac{\bar{z}\Delta t}{\rho}\partial_y p^{n+1} = \bar{\sigma}^{n+1}_{22,0} + 2ik_x\mu v_1^{n+1} - \bar{z}\Delta t\big[\dot{\bar{v}}^{n+1}_{2,0} \\ +\nu\left(k_x^2 v_2^{n+1} + ik_x\partial_y v_1^{n+1}\right)\big], \qquad y = 0, \end{aligned} \tag{5.7}$$

again using $\partial_y v_2^{n+1} = -ik_x v_1^{n+1}$. The acceleration of the solid on the interface, denoted by $\dot{\bar{v}}^{n+1}_{2,0}$ in (5.7), is taken to be $\dot{\bar{v}}^{n+1}_{2,0} = (\bar{v}^{n+1}_{2,0} - \bar{v}^n_{2,0})/\Delta t$. After solving for

the fluid velocity and pressure, interface quantities from the fluid are obtained using

$$v_{m,f}^{n+1} = v_m^{n+1}, \quad m = 1, 2, \qquad p_f^{n+1} = p^{n+1},$$
$$\sigma_{12,f}^{n+1} = \mu\left(\partial_y v_1^{n+1} + ik_x v_2^{n+1}\right), \qquad \sigma_{22,f}^{n+1} = -p^{n+1} + 2\mu\partial_y v_2^{n+1},$$

where all fluid quantities on the right-hand side are evaluated at $y = 0$. The interface velocity and traction are projected from fluid and solid values using (3.6). These projections reduce to

$$v_m^I = \frac{z_f}{z_f + \bar{z}} v_{m,f}^{n+1} + \frac{\bar{z}}{z_f + \bar{z}} \bar{v}_{m,0}^{n+1} + \frac{1}{z_f + \bar{z}} (\bar{\sigma}_{m2,0}^{n+1} - \sigma_{m2,f}^{n+1}), \tag{5.8a}$$

$$\sigma_{m2}^I = \frac{z_f^{-1}}{z_f^{-1} + \bar{z}^{-1}} \sigma_{m2,f}^{n+1} + \frac{\bar{z}^{-1}}{z_f^{-1} + \bar{z}^{-1}} \bar{\sigma}_{m2,0}^{n+1} + \frac{1}{z_f^{-1} + \bar{z}^{-1}} (\bar{v}_{m,0}^{n+1} - v_{m,f}^{n+1}), \tag{5.8b}$$

where $m = 1, 2$. Finally, the ghost points at $j = 1$ for the incoming solid characteristics are set using

$$a_{m,1}^{n+1} = \sigma_{m2}^I + \bar{z} v_m^I, \qquad m = 1, 2, \tag{5.9}$$

which is a first-order accurate approximation (consistent with the order of accuracy of the upwind scheme).

We next consider the coupling conditions for the TP and ATP schemes. These conditions can be obtained from the coupling conditions for the AMP scheme in the limits of heavy ($\bar{z} \to \infty$) and light ($\bar{z} \to 0$) solids. For the AMP algorithm, the fluid velocity and pressure conditions are given in (5.4), (5.5) and (5.7), while the final interface values are defined by the projections in (5.8). For the TP algorithm ($\bar{z} \to \infty$), the AMP conditions in (5.4) and (5.5) reduce to Dirichlet conditions on the fluid velocity given by

$$v_m^{n+1} = \bar{v}_{m,0}^{n+1}, \qquad y = 0, \qquad m = 1, 2.$$

The pressure condition in (5.7) becomes a Neumann condition given by

$$\partial_y p^{n+1} = -\dot{\bar{v}}_{2,0}^{n+1} - \nu\left(k_x^2 v_2^{n+1} + ik_x \partial_y v_1^{n+1}\right), \qquad y = 0. \tag{5.10}$$

For the TP scheme, the interface velocity is taken to be the solid velocity, $v_m^I = \bar{v}_{m,0}^{n+1}$, and the interface traction is taken to be the fluid traction, $\sigma_{m2}^I = \sigma_{m2,f}^{n+1}$, $m = 1, 2$.

For the ATP scheme, we consider the light-solid limit ($\bar{z} \to 0$) of the AMP conditions. In this limit, the condition on the outgoing solid tangential characteristic in (5.4) reduces to a Neumann condition for the velocity given by

$$\mu\left(ik_x v_2^{n+1} + \partial_y v_1^{n+1}\right) = \bar{\sigma}_{12,0}^{n+1}, \qquad y = 0, \tag{5.11}$$

while the condition in (5.5) becomes

$$v_2^{n+1} = V^p(v_2^{n+1}), \qquad y = 0, \tag{5.12}$$

where $V^p(v_2^{n+1})$ is given by (5.6). Using (5.2b), it can be shown that the condition in (5.12) can be replaced by

$$\partial_y\left(ik_x v_1^{n+1} + \partial_y v_2^{n+1}\right) = 0, \qquad y = 0, \tag{5.13}$$

which is equivalent to setting the fluid velocity to be divergence-free on the interface. For the ATP scheme, the pressure condition in (5.7) reduces to

$$-p^{n+1} + 2\mu\partial_y v_2^{n+1} = \bar{\sigma}_{22,0}^{n+1}, \qquad y = 0. \tag{5.14}$$

For the ATP scheme, the interface velocity is taken to be the fluid velocity, $v_m^I = v_{m,f}^{n+1}$, and the interface traction is taken to be the solid traction, $\sigma_{m2}^I = \bar{\sigma}_{m2,0}^{n+1}$, $m = 1, 2$.

5.4. Stability analysis. In order to assess the stability of the AMP, TP and ATP schemes, we search for normal mode solutions to the discrete evolution equations. In the fluid, solutions are of the form

$$v_m^n(y) = A^n \tilde{v}_m(y), \qquad p^n(y) = A^n \tilde{p}(y), \qquad m = 1, 2, \tag{5.15}$$

where A is an amplification factor. Note that while it is not necessary to assume that the amplification factors for velocity and pressure are the same in their initial forms, the condition that these forms satisfy the momentum equations in (5.2a)–(5.2b) would immediately imply that amplification factors are equal. Substituting (5.15) into (5.2) and integrating gives

$$\tilde{v}_1(y) = v_{1,f}^0 e^{-\gamma|k_x|y} - \frac{ip_f^0}{\mu k_x A(\gamma^2 - 1)} \left(e^{-|k_x|y} - e^{-\gamma|k_x|y} \right), \tag{5.16a}$$

$$\tilde{v}_2(y) = v_{2,f}^0 e^{-\gamma|k_x|y} + \frac{p_f^0}{\mu|k_x| A(\gamma^2 - 1)} \left(e^{-|k_x|y} - e^{-\gamma|k_x|y} \right), \tag{5.16b}$$

$$\tilde{p}(y) = p_f^0 e^{-|k_x|y}, \tag{5.16c}$$

where $\mu = \rho\nu$, $\gamma = \sqrt{1 + (1 - 1/A)/\Lambda}$ and $\Lambda = \nu k_x^2 \Delta t$. Here, Λ represents the viscous CFL number and we have imposed boundedness of the solution in (5.16) as $y \to \infty$. The constants, $v_{m,f}^0$ and p_f^0, are obtained by imposing the appropriate boundary conditions at $y = 0$, namely, (5.4), (5.5) and (5.7) for the case of the AMP scheme. For the TP scheme, the three constraints are the two boundary conditions for the components of the velocity in (5.11) and the condition on the pressure in (5.10), while the ATP scheme uses the boundary conditions in (5.11), (5.13) and (5.14).

Having found solutions for the velocity and pressure of the fluid, these solutions can be used (along with the appropriate boundary conditions at $y = 0$ for the AMP, TP or ATP coupling) to eliminate the fluid variables on the boundary in favor of the solid variables. The issue of stability, then, reduces to examining the behavior of the evolution equations for the solid with the appropriate boundary conditions. Solutions of these evolution equations are sought in the form

$$\mathbf{a}_j^n = \phi^j A^n \tilde{\mathbf{r}}, \qquad \mathbf{a}_j^n = [a_{1,j}^n\,,\, b_{1,j}^n\,,\, a_{2,j}^n\,,\, b_{2,j}^n\,,\, d_j^n]^T, \tag{5.17}$$

where ϕ is a spatial eigenvalue and $\tilde{\mathbf{r}}$ is a constant eigenvector. The scheme is said to be weakly stable if there are no non-trivial solutions with $|A| > 1$. Our strategy for determining regions of stability will be to search for unstable modes with $|A| > 1$, and then identify regions of the parameter space where no non-trivial solutions exist. To do this, we begin by finding the general solution for the spatial grid functions satisfying the discrete equations and regularity condition as $j \to -\infty$, assuming $|A| > 1$. We then apply the conditions at the interface to determine whether non-trivial solutions exist.

Substitution of the normal mode ansatz (5.17) into the evolution equations for the solid in (5.3), yields a 5×5 homogeneous system of the form $\mathcal{F}(\phi)\tilde{\mathbf{r}} = 0$. Nontrivial solutions exist if

$$f(\phi) \stackrel{\text{def}}{=} \det(\mathcal{F}(\phi)) = (1-A)\left(\eta(\phi)\eta(1/\phi) + (A\lambda_x)^2\right)^2 = 0, \tag{5.18}$$

where $\eta(\phi) \stackrel{\text{def}}{=} 1 - A + \lambda_y(\phi - 1)$, $\lambda_x \stackrel{\text{def}}{=} \bar{c}|k_x|\Delta t$ and $\lambda_y \stackrel{\text{def}}{=} \bar{c}\Delta t/\Delta y$. Since we seek unstable modes with $|A| > 1$, the determinant condition in (5.18) is satisfied only when $\eta(\phi)\eta(1/\phi) = -(A\lambda_x)^2$. This leads to the roots given by

$$\phi_\pm = \xi \pm \sqrt{\xi^2 - 1}, \qquad \xi = 1 - \frac{(A\lambda_x)^2 + (1-A)^2}{2\lambda_y(1 - A - \lambda_y)}.$$

Note that the product of the roots is equal to one (i.e. $\phi_+\phi_- = 1$). Since we are searching for solutions that are bounded as $j \to -\infty$, we are only interested in the root with modulus greater than one.

Lemma: *If $|A| > 1$ and if λ_x and λ_y are chosen to satisfy a CFL condition, then there is precisely one root, either ϕ_+ or ϕ_-, denoted by ϕ_* that has magnitude strictly greater than one, i.e. $|\phi_*| > 1$.*

This result follows from a similar argument to that given in [18]. We first consider the scheme applied to the pure initial-value problem (Cauchy problem). Setting $\phi = e^{i\vartheta}$ in (5.18), we determine a region of the (λ_x, λ_y) plane for which $|A| \le 1$ for all $\vartheta \in [0, 2\pi]$. This stable region is found numerically, and it includes a region satisfying a reasonable CFL restriction, namely $\lambda_x^2 + \lambda_y^2 \le 1$ (see [25]). Next, since $|A| \le 1$ when $|\phi| = 1$, we have that $|\phi| \ne 1$ when $|A| > 1$. Thus, if $|A| > 1$ and if (λ_x, λ_y) remains within the CFL restriction, then ϕ cannot cross the unit circle, $|\phi| = 1$, as (λ_x, λ_y) vary. It is therefore only necessary to prove that the lemma holds for one set of parameters. For $\lambda_x = 0$, the discretization reduces to four uncoupled upwind schemes for linear advection. In this case, equation (5.18) is equivalent to $\eta(\phi)\eta(1/\phi) = 0$, which has solutions $\phi_+ = (A - 1 + \lambda_y)/\lambda_y$ and $\phi_- = 1/\phi_+$. When $|A| > 1$ and $\lambda_y \in (0, 1]$, $|\phi_+| > 1$ and therefore $\phi_* = \phi_+$. Thus, the condition holds for all (λ_x, λ_y) provided the CFL condition is satisfied.

The two eigenvectors associated with $\phi = \phi_*$ lead to bounded solutions given by

$$a^n_{1,j} = k_1 \mathrm{sgn}(k_x)\frac{\eta(1/\phi_*)}{iA\lambda_x}\phi_*^j A^n, \qquad b^n_{1,j} = -k_2 \mathrm{sgn}(k_x)\frac{\eta(\phi_*)}{iA\lambda_x}\phi_*^j A^n,$$
$$a^n_{2,j} = k_2\phi_*^j A^n, \qquad b^n_{2,j} = k_1\phi_*^j A^n,$$

where k_1 and k_2 are constants to be determined by the two interface conditions in (5.9). The application of these interface conditions leads to a 2×2 homogeneous system of the form $\mathcal{G}(A)\mathbf{k} = 0$. Solutions for the amplification factor A are roots of the transcendental equation given by

$$g(A) \stackrel{\text{def}}{=} \det(\mathcal{G}(A)) = 0.$$

These roots depend on the choice of interface coupling (AMP, TP or ATP) and four dimensionless parameters $(\Lambda, Z, \lambda_x, \lambda_y)$, where $Z \stackrel{\text{def}}{=} \mu|k_x|/\bar{z}$. (Further details are given in [25].)

Proving stability of the partitioned scheme for a choice of the interface coupling and dimensional parameters is equivalent to showing that no roots of $g(A) = 0$ exist

such that $|A| > 1$. The number of roots with $|A| > 1$ can be assessed using the argument principle. Define

$$\mathcal{P} \stackrel{\text{def}}{=} \frac{1}{2\pi i} \oint_{|\zeta|=1} \frac{G'(\zeta)}{G(\zeta)}\, d\zeta, \qquad G(\zeta) = g(1/\zeta).$$

There are branch points of $G(\zeta)$ in the region $|\zeta| > 1$, and a single-valued branch of $G(\zeta)$ can be defined so that its branch cuts lie outside the unit disk. Using this definition, the only singularity of $G(\zeta)$ in the region $|\zeta| \leq 1$ is a pole of order 2 at the origin, and thus $\mathcal{P} = N - 2$, where N corresponds to the number of roots of $g(A)$ with $|A| > 1$.

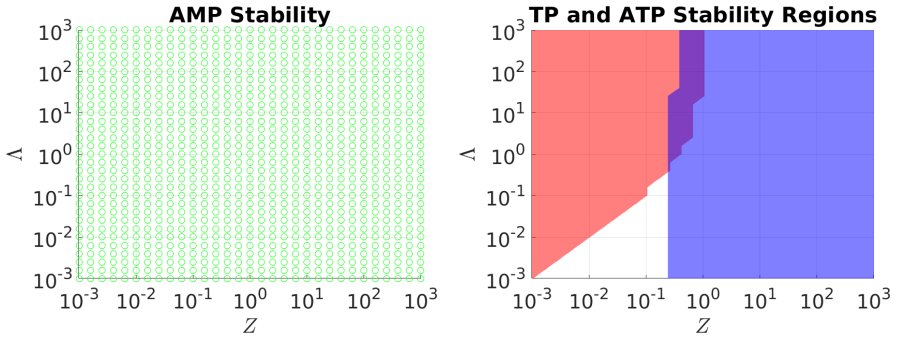

FIG. 2. *Left: Green circles represent points for which the AMP algorithm is stable in the CFL region $\lambda_x^2 + \lambda_y^2 \leq 1$. Right: stability regions for the TP (red) and ATP (blue) schemes.*

An analytic evaluation of the integral for $\mathcal{P}$ is unavailable, and so we consider a numerical evaluation. The four-dimensional parameter space (Z,Λ,λ_x,λ_y) is discretized on a $31\times31\times20\times20$ array. The parameters Z and Λ are equally spaced on a logarithmic scale on the interval $[10^{-3}, 10^3]$, while λ_x and λ_y are equally spaced on the interval $[0.05, 0.95]$. At each grid point, $\mathcal{P}$ is computed numerically with $|\mathcal{P} + 2| \leq \delta$ corresponding to stability, where δ is a small parameter taken to be 10^{-5}. The results of this computation are shown in Figure 2 for the AMP, TP and ATP schemes. A grid point in the (Λ, Z) plane is marked as stable if the computations of $\mathcal{P}$ for all values of λ_x and λ_y in the search region are stable. The point is marked as unstable otherwise. The results shown in the left plot indicate that the AMP scheme applied to the viscous model problem is stable for all points in the (Λ, Z) plane, whereas the results shown in the right plot indicate that the TP and ATP schemes have large regions of instability. For example, the region in red shows the stable region for the TP scheme, which occurs for heavy solids (Z small) and coarser meshes (Λ large). The stability region for the ATP scheme shown in blue corresponds to light solids (Z large). The following theorem summarizes the results for the AMP scheme.

Theorem: *The AMP scheme applied to viscous model problem is weakly stable $|A| \leq 1$ provided $\lambda_x^2 + \lambda_y^2 \leq 1$, which gives the usual CFL-type time-step restriction*

$$\Delta t \leq \frac{1}{\bar{c}} \left[\frac{1}{\Delta y^2} + k_x^2 \right]^{1/2}.$$

This is a sufficient but not a necessary condition. The proof follows from the argument principle and a numerical evaluation of $\mathcal{P}$.

6. Numerical results for an elastic piston. We now present numerical results for two FSI problems to verify the accuracy and stability of the AMP scheme. The two FSI problems considered involve the interaction of a fluid column with an elastic piston. In the first problem, we examine longitudinal motion of the piston (which primarily involves added-mass effects), while transverse motion of the piston (which primarily involves added-damping effects) is considered in the second problem. Exact solutions are found for both FSI problems, and these are used to verify the accuracy and stability of the AMP algorithm for a range of the problem parameters.

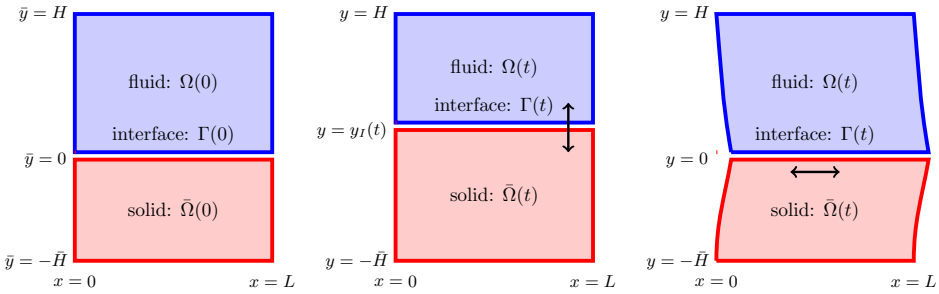

FIG. 3. *FSI problem coupling an incompressible viscous fluid and an elastic piston: Configuration at $t = 0$ (left), lonngitudinal motion for $t > 0$ (middle) and shear motion for $t > 0$ (right).*

Longitudinal motion of an elastic piston. The geometry of the elastic piston problem is shown in Figure 3. The plot on the left shows the configuration at $t = 0$. The fluid occupies the physical domain between $y = 0$ and $y = H$ initially, while the solid lies in its reference domain between $\bar{y} = -\bar{H}$ and $\bar{y} = 0$. It is assumed that there is no dependence in the x-direction so that the fluid-solid interface remains flat at a position $y = y_I(t)$ as shown in the plot on the right. In the fluid domain, $\Omega(t)$, it is assumed that the horizontal component of velocity v_1 is zero, and thus the vertical component v_2 is a function of t alone according to the continuity equation.

Solutions to this FSI problem can be constructed for a specified motion of the fluid solid interface, see [25] for more details. We choose an interface position $y_I(t)$ that oscillates in the vertical direction with frequency ω and an amplitude a given by

$$y_I(t) = a\sin(\omega t), \qquad a = 2\alpha\sin(\omega\bar{H}/\bar{c}_p).$$

Numerical results are obtained for the case $H = 1, \rho = 1$ and $\mu = 0.01$ for the fluid, and using $\bar{H} = 0.5$ and $\bar{\mu} = \bar{\lambda} = \bar{\rho} = \delta$ for the solid. The interface position is specified by $a = 0.1$ and $\omega = 2\pi$. The density ratio, $\bar{\rho}/\rho = \delta$, is taken to be 10^{-3}, 1 and 10^3, representing FSI problems with light, moderate and heavy solids, respectively. Numerical solutions are computed using the AMP algorithm on a two-dimensional rectangular configuration (as shown in Figure 3) with periodic boundary conditions taken at $x = 0$ and $x = L$ consistent with a one-dimensional solution. Table 1 gives the maximum-norm errors for solutions computed using the AMP algorithm at $t_{\text{final}} = 0.6$ with grid resolutions $h = 1/(20j)$ for $j = 1, 2, 4, 8$. The errors in the table indicate that the solution is converging at second-order accuracy.

Transverse motion of an elastic piston. Exact solutions can also be constructed for an FSI problem involving transverse motion of an elastic piston, see Figure 3. For this case, the vertical components of the fluid velocity and solid displacement are taken to be zero, while the corresponding horizontal components are assumed to be functions of y and t alone. As a result, the interface only moves horizontally so that

TABLE 1

Longitudinal motion of an elastic piston: Maximum-norm errors and convergence ratios of the numerical solution at $t_{\text{final}} = 0.6$ computed using the AMP algorithm for $\bar{\rho}/\rho = \delta = 10^3$, 1 and 10^{-3}.

Heavy solid ($\delta = 10^3$):

h	$E^{(p)}$	r	$E^{(\mathbf{v})}$	r	$E^{(\bar{\mathbf{u}})}$	r	$E^{(\bar{\mathbf{v}})}$	r	$E^{(\bar{\boldsymbol{\sigma}})}$	r
1/ 20	6.0e-04		5.9e-05		4.0e-05		5.9e-05		1.9e-01	
1/ 40	1.4e-04	4.2	1.7e-05	3.5	9.6e-06	4.2	1.7e-05	3.5	4.5e-02	4.2
1/ 80	3.4e-05	4.1	4.4e-06	3.8	2.3e-06	4.1	4.4e-06	3.8	1.1e-02	4.1
1/160	8.5e-06	4.1	1.1e-06	3.9	5.8e-07	4.1	1.1e-06	3.9	2.7e-03	4.1

Medium solid ($\delta = 1$):

h	$E^{(p)}$	r	$E^{(\mathbf{v})}$	r	$E^{(\bar{\mathbf{u}})}$	r	$E^{(\bar{\mathbf{v}})}$	r	$E^{(\bar{\boldsymbol{\sigma}})}$	r
1/ 20	1.8e-05		4.9e-05		1.2e-05		4.9e-05		5.0e-05	
1/ 40	7.5e-06	2.4	1.2e-05	4.0	3.0e-06	4.2	1.2e-05	4.0	1.3e-05	3.7
1/ 80	2.3e-06	3.3	3.0e-06	4.0	7.1e-07	4.1	3.0e-06	4.0	3.6e-06	3.8
1/160	6.3e-07	3.6	7.4e-07	4.0	1.8e-07	4.1	7.4e-07	4.0	9.2e-07	3.9

Light solid ($\delta = 10^{-3}$):

h	$E^{(p)}$	r	$E^{(\mathbf{v})}$	r	$E^{(\bar{\mathbf{u}})}$	r	$E^{(\bar{\mathbf{v}})}$	r	$E^{(\bar{\boldsymbol{\sigma}})}$	r
1/ 20	8.0e-07		6.5e-07		3.3e-06		2.4e-05		1.3e-07	
1/ 40	2.4e-07	3.3	1.6e-07	4.0	5.3e-07	6.3	4.2e-06	5.7	3.4e-08	3.9
1/ 80	6.6e-08	3.7	4.1e-08	4.0	8.9e-08	5.9	8.3e-07	5.0	8.8e-09	3.9
1/160	1.7e-08	3.8	1.0e-08	4.0	2.3e-08	3.8	1.8e-07	4.5	2.2e-09	4.0

$y_I(t) = y_I(0) = 0$, and the solid reference coordinate $\bar{y}$ is equivalent to the physical coordinate y.

For this problem, the equations governing the horizontal components of the fluid velocity and solid displacement reduce to $v_{1,t} = \nu v_{1,yy}$, for $0 < y < H$, and $\bar{u}_{1,tt} = \bar{c}_s^2 \bar{u}_{1,yy}$, for $-\bar{H} < y < 0$, and there are time periodic solutions with $v_1(y,t) = \hat{v}_1(y)e^{i\omega t}$ and $\bar{u}_1(y,t) = \hat{\bar{u}}_1(y)e^{i\omega t}$ for certain values of the eigenvalue ω (see [25] for further details).

Solutions to this problem are computed for selected values of ω (as noted in Table 2) for $H = 1$, $\bar{H} = 0.5$, $\rho = 1$ and $\mu = 0.1$, and for different values of $\delta = \bar{\rho} = \bar{\mu} = \bar{\lambda}$. The magnitude of the interface displacement in the x-direction at $t = 0$ is taken as $\bar{u}_0 = 0.1$. Table 2 gives the maximum-norm errors for solutions computed using the AMP algorithm. The results are presented for solutions at $t_{\text{final}} = 0.3$ using grid resolutions $h = 1/(20j)$, for $j = 1, 2, 4, 8$. The errors in the table indicate that the solution is converging at second-order accuracy.

7. Conclusions. A stable added-mass partitioned (AMP) algorithm was developed for fluid-structure interaction problems involving viscous incompressible fluids and compressible elastic solids. The new algorithm is stable, without sub-time-step iterations, for both heavy and very light solids thus effectively suppresses both added-mass and added-damping effects. The fluid is advanced using a fractional-step IMEX scheme with the viscous terms treated implicitly. Key elements of the new AMP scheme are a Robin interface condition for the pressure and an impedance-weighted interface projection based on a new form for the fluid impedance. The fluid impedance is derived from the analysis of a carefully chosen FSI model problem. Stability of the AMP scheme is analyzed for a related model problem. A set of *elastic-piston* benchmark problems was developed to verify the stability and accuracy of the AMP scheme. These solutions are exact and include finite interface deformations either normal or tangential to the surface.

TABLE 2

Transverse motion of an elastic piston: Maximum-norm errors and convergence ratios of the numerical solution at $t_{\text{final}} = 0.3$ computed using the AMP algorithm for $\bar{\rho}/\rho = \delta = 10^3$, 1 and 10^{-3}.

Heavy solid ($\delta = 10^3$, $\omega = 3.141 + i\,7.930 \cdot 10^{-4}$):

h	$E^{(p)}$	r	$E^{(\mathbf{v})}$	r	$E^{(\bar{\mathbf{u}})}$	r	$E^{(\bar{\mathbf{v}})}$	r	$E^{(\bar{\boldsymbol{\sigma}})}$	r
1/ 20	6.0e-04		5.9e-05		4.0e-05		5.9e-05		1.9e-01	
1/ 40	1.4e-04	4.2	1.7e-05	3.5	9.6e-06	4.2	1.7e-05	3.5	4.5e-02	4.2
1/ 80	3.4e-05	4.1	4.4e-06	3.8	2.3e-06	4.1	4.4e-06	3.8	1.1e-02	4.1
1/160	8.5e-06	4.1	1.1e-06	3.9	5.8e-07	4.1	1.1e-06	3.9	2.7e-03	4.1

Medium solid ($\delta = 1$, $\omega = 2.351 + i\,5.433 \cdot 10^{-1}$):

h	$E^{(p)}$	r	$E^{(\mathbf{v})}$	r	$E^{(\bar{\mathbf{u}})}$	r	$E^{(\bar{\mathbf{v}})}$	r	$E^{(\bar{\boldsymbol{\sigma}})}$	r
1/ 20	1.8e-05		4.9e-05		1.2e-05		4.9e-05		5.0e-05	
1/ 40	7.5e-06	2.4	1.2e-05	4.0	3.0e-06	4.2	1.2e-05	4.0	1.3e-05	3.7
1/ 80	2.3e-06	3.3	3.0e-06	4.0	7.1e-07	4.1	3.0e-06	4.0	3.6e-06	3.8
1/160	6.3e-07	3.6	7.4e-07	4.0	1.8e-07	4.1	7.4e-07	4.0	9.2e-07	3.9

Light solid ($\delta = 10^{-3}$, $\omega = 6.285 + i\,1.784 \cdot 10^{-3}$):

h	$E^{(p)}$	r	$E^{(\mathbf{v})}$	r	$E^{(\bar{\mathbf{u}})}$	r	$E^{(\bar{\mathbf{v}})}$	r	$E^{(\bar{\boldsymbol{\sigma}})}$	r
1/ 20	8.0e-07		6.5e-07		3.3e-06		2.4e-05		1.3e-07	
1/ 40	2.4e-07	3.3	1.6e-07	4.0	5.3e-07	6.3	4.2e-06	5.7	3.4e-08	3.9
1/ 80	6.6e-08	3.7	4.1e-08	4.0	8.9e-08	5.9	8.3e-07	5.0	8.8e-09	3.9
1/160	1.7e-08	3.8	1.0e-08	4.0	2.3e-08	3.8	1.8e-07	4.5	2.2e-09	4.0

The present AMP algorithm assumes a linear elastic constitutive model for the finite deformation of the solid. This was done as a first step towards an extension to nonlinear hyperelastic models, such as neo-Hookean or Saint Venant-Kirchoff. Such an extension was considered previously in [4] for FSI problems involving inviscid compressible fluids. In that paper, the AMP interface conditions used a linearization of the nonlinear model locally about points along the interface, and so the linear elastic model considered here should provide useful information for an analogous extension to FSI problems coupling viscous incompressible fluids and nonlinear solids. Such an extension is planned for future work.

REFERENCES

[1] D. APPELÖ, J. W. BANKS, W. D. HENSHAW, AND D. W. SCHWENDEMAN, *Numerical methods for solid mechanics on overlapping grids: Linear elasticity*, J. Comput. Phys., 231 (2012), pp. 6012–6050.

[2] S. BADIA, F. NOBILE, AND C. VERGARA, *Fluid–structure partitioned procedures based on Robin transmission conditions*, J. Comput. Phys., 227 (2008), pp. 7027–7051, https://doi.org/http://dx.doi.org/10.1016/j.jcp.2008.04.006.

[3] S. BADIA, F. NOBILE, AND C. VERGARA, *Robin-Robin preconditioned Krylov methods for fluid–structure interaction problems*, CMAME, 198 (2009), pp. 2768–2784.

[4] J. W. BANKS, W. D. HENSHAW, A. KAPILA, AND D. W. SCHWENDEMAN, *An added-mass partitioned algorithm for fluid-structure interactions of compressible fluids and nonlinear solids*, J. Comput. Phys., 305 (2016), pp. 1037–1064.

[5] J. W. BANKS, W. D. HENSHAW, AND D. W. SCHWENDEMAN, *Deforming composite grids for solving fluid structure problems*, J. Comput. Phys., 231 (2012), pp. 3518–3547, https://doi.org/10.1016/j.jcp.2011.12.034.

[6] J. W. BANKS, W. D. HENSHAW, AND D. W. SCHWENDEMAN, *An analysis of a new stable partitioned algorithm for FSI problems. Part I: Incompressible flow and elastic solids*, J. Comput. Phys., 269 (2014), pp. 108–137.

[7] J. W. BANKS, W. D. HENSHAW, AND D. W. SCHWENDEMAN, *An analysis of a new stable partitioned algorithm for FSI problems. Part II: Incompressible flow and structural shells*,

J. Comput. Phys., 268 (2014), pp. 399–416.

[8] J. W. Banks, W. D. Henshaw, D. W. Schwendeman, and Q. Tang, *A stable partitioned FSI algorithm for rigid bodies and incompressible flow. Part I: Model problem analysis.*, J. Comput. Phys., 343 (2017), pp. 432–468.

[9] J. W. Banks, W. D. Henshaw, D. W. Schwendeman, and Q. Tang, *A stable partitioned FSI algorithm for rigid bodies and incompressible flow. Part II: General formulation*, J. Comput. Phys., 343 (2017), pp. 469–500.

[10] J. W. Banks, W. D. Henshaw, D. W. Schwendeman, and Q. Tang, *A stable partitioned FSI algorithm for rigid bodies and incompressible flow in three dimensions*, J. Comput. Phys., 373 (2018), pp. 455–492.

[11] J. W. Banks and B. Sjögreen, *A normal mode stability analysis of numerical interface conditions for fluid/structure interaction*, Commun. Comput. Phys., 10 (2011), pp. 279–304.

[12] S. Basting, A. Quaini, S. Čanić, and R. Glowinski, *Extended ALE method for fluid-structure interaction problems with large structural displacements*, Journal of Computational Physics, 331 (2017), pp. 312 – 336, https://doi.org/https://doi.org/10.1016/j.jcp.2016.11.043.

[13] M. A. Fernández and M. Landajuela, *Fully decoupled time-marching schemes for incompressible fluid/thin-walled structure interaction*, Rapport de recherche RR-8425, INRIA, Jan. 2014.

[14] M. A. Fernández, J. Mullaert, and M. Vidrascu, *Explicit Robin-Neumann schemes for the coupling of incompressible fluids with thin-walled structures*, Comput. Method. Appl. Mech. Engrg., 267 (2013), pp. 566–593.

[15] M. A. Fernández, J. Mullaert, and M. Vidrascu, *Generalized Robin-Neumann explicit coupling schemes for incompressible fluid–structure interaction: stability analysis and numerics*, Int. J. Numer. Meth. Eng., (2014), https://doi.org/10.1002/nme.4785.

[16] L. Gerardo-Giorda, F. Nobile, and C. Vergara, *Analysis and optimization of Robin-Robin partitioned procedures in fluid–structure interaction problems*, SIAM J. Numer. Anal., 48 (2010), pp. 2091–2116.

[17] W. D. Henshaw and N. A. Petersson, *A split-step scheme for the incompressible Navier-Stokes equations*, in Numerical Simulation of Incompressible Flows, M. M. Hafez, ed., World Scientific, 2003, pp. 108–125.

[18] H. O. Kreiss, *Difference approximations for the initial-boundary value problem for hyperbolic differential equations*, Numerical Solutions of Nonlinear Differential Equations, (1996), pp. 141–166.

[19] U. Küttler and W. A. Wall, *Fixed-point fluid–structure interaction solvers with dynamic relaxation*, Computational Mechanics, 43 (2008), pp. 61–72, https://doi.org/10.1007/s00466-008-0255-5.

[20] L. Li, W. D. Henshaw, J. W. Banks, D. W. Schwendeman, and G. A. Main, *A stable partitioned FSI algorithm for incompressible flow and deforming beams*, J. Comput. Phys., 312 (2016), pp. 272–306.

[21] M. Mehl, B. Uekermann, H. Bijl, D. Blom, B. Gatzhammer, and A. van Zuijlen, *Parallel coupling numerics for partitioned fluid-structure interaction simulations*, Computers & Mathematics with Applications, 71 (2016), pp. 869 – 891, https://doi.org/https://doi.org/10.1016/j.camwa.2015.12.025.

[22] D. P. Mok, W. A. Wall, and E. Ramm, *Accelerated iterative substructuring schemes for instationary fluid structure interaction*, in Computational Fluid and Solid Mechanics, K. Bathe, ed., Elsevier, 2001, pp. 1325–1328.

[23] F. Nobile, M. Pozzoli, and C. Vergara, *Inexact accurate partitioned algorithms for fluid–structure interaction problems with finite elasticity in haemodynamics*, Journal of Computational Physics, 273 (2014), pp. 598 – 617, https://doi.org/http://dx.doi.org/10.1016/j.jcp.2014.05.020.

[24] D. A. Serino, J. W. Banks, W. D. Henshaw, and D. W. Schwendeman, *A stable added-mass partitioned (AMP) algorithm for elastic solids and incompressible flow*, preprint arXiv:1812.05208, 2019. submitted for publication.

[25] D. A. Serino, J. W. Banks, W. D. Henshaw, and D. W. Schwendeman, *A stable added-mass partitioned (AMP) algorithm for elastic solids and incompressible flow: Model problem analysis*, preprint arXiv:1812.03192, 2019. submitted for publication.

[26] Y. Wang, A. Quaini, and S. Čanić, *A higher-order discontinuous Galerkin/arbitrary Lagrangian Eulerian partitioned approach to solving fluid–structure interaction problems with incompressible, viscous fluids and elastic structures*, Journal of Scientific Computing, 76 (2018), pp. 481–520, https://doi.org/10.1007/s10915-017-0629-y.